



HAL
open science

Mechanism of reactant and product dissociation from the anthrax edema factor: A locally enhanced sampling and steered molecular dynamics study

Leandro Martínez, Thérèse Malliavin, Arnaud Blondel

► To cite this version:

Leandro Martínez, Thérèse Malliavin, Arnaud Blondel. Mechanism of reactant and product dissociation from the anthrax edema factor: A locally enhanced sampling and steered molecular dynamics study. *Proteins - Structure, Function and Bioinformatics*, 2011, 79 (5), pp.1649-1661. 10.1002/prot.22991 . pasteur-02510854

HAL Id: pasteur-02510854

<https://pasteur.hal.science/pasteur-02510854>

Submitted on 7 Apr 2020

HAL is a multi-disciplinary open access archive for the deposit and dissemination of scientific research documents, whether they are published or not. The documents may come from teaching and research institutions in France or abroad, or from public or private research centers.

L'archive ouverte pluridisciplinaire **HAL**, est destinée au dépôt et à la diffusion de documents scientifiques de niveau recherche, publiés ou non, émanant des établissements d'enseignement et de recherche français ou étrangers, des laboratoires publics ou privés.

Mechanism of reactant and product dissociation from
the Anthrax Edema Factor: a Locally Enhanced
Sampling and Steered Molecular Dynamics Study

Leandro Martínez ^{*†} Thérèse E. Malliavin ^{*} Arnaud Blondel ^{*}

December 1, 2010

Short title: Ligand dissociation in EF

Keywords: adenylyl cyclase, ion binding, ATP, cyclic-AMP, simulation

^{*}Unité de Bioinformatique Structurale, URA CNRS 2185, Institut Pasteur, 25, rue du Dr Roux, F-75015 Paris, France.

[†]Current affiliation: Instituto de Física de São Carlos, Universidade de São Paulo. Av. Trabalhador São-carlense 400, 13566-590 São Carlos, SP, Brasil. e-mail: leandro@ifsc.usp.br

Abstract

The Anthrax Edema Factor is a toxin overproducing cyclic adenosine monophosphate (cAMP) and pyrophosphate (PPi) from ATP. Here, mechanisms of dissociation of ATP and products (cAMP, PPi) from the active site are studied using Locally Enhanced Sampling (LES) and Steered Molecular Dynamics (SMD) simulations. Various substrate conformations and ionic binding modes found in crystallographic structures are considered. LES simulations show that PPi and cAMP dissociate through different solvent accessible cavities, while ATP dissociation requires significant active site exposure to solvent. The ionic content of the active site directly affects the dissociation of ATP and products. Only one ion dissociates along with ATP in the two-Mg²⁺ binding site, suggesting that the other ion binds EF prior to ATP association. Dissociation of reaction products cAMP and PPi is impaired by direct electrostatic interactions between products and Mg²⁺ ions. This provides an explanation for the inhibitory effect of high Mg²⁺ concentrations on EF enzymatic activity. Breaking of electrostatic interactions is dependent on a competitive binding of water molecules to the ions, and thus on the solvent accessibility of the active site. Consequently, product dissociation seems to be a two-step process. First, ligands are progressively solvated while preserving the most important electrostatic interactions, in a process that is dependent on the flexibility of the active site. Second, breakage of the electrostatic bonds follows, and ligands diffuse into solvent. In agreement with this mechanism, product protonation facilitates dissociation.

1 Introduction

The anthrax Edema Factor (EF) is one of three major toxins secreted by *Bacillus anthracis* bacteria. When EF enters the host cell, it forms a complex with calmodulin (CaM). A large conformational transition of EF [1] is necessary to insert CaM between two EF domains. This transition activates EF as an adenylyl cyclase, converting ATP into cyclic-AMP (cAMP) and Pyrophosphate (PPi).

EF enzymatic activity depends on Ca^{2+} and Mg^{2+} ions. Association of Ca^{2+} with the C-terminal lobe of CaM is essential for stability of the complex [2–4]. Besides, the cyclization reaction depends on Mg^{2+} ions in the active site, as in many other enzymes which convert ATP to cAMP and Pyrophosphate [5, 6]. These ions stabilize charges of nucleophilic groups and of products [6–8] and, thus, the transition state.

Wei-Jen Tang and co-workers studied exhaustively EF structures: isolated EF, EF bound to CaM, EF-CaM complexed with substrate analogs, and EF-CaM complexed with products. These structures display different ionic binding modes for Ca^{2+} and Mg^{2+} [1, 9, 10] and provide a comprehensive view of EF structure-function relationships. Functional studies, site-directed mutagenesis and kinetic analysis provided additional information [7, 11]. However, as catalysis is a dynamical process, computational studies would provide a better understanding of the EF enzymatic activity, as it was suggested in the conclusions of [10].

The presence of one or two metal ions in the catalytic site of EF is particularly contro-

versial. The first crystal structure obtained (PDB entry: 1K90) contained EF complexed with CaM and 3'-deoxy-ATP, in presence of a single metal ion [1]. This cation was in a central position in the active site and was identified as an Ytterbium(III) coordinated by Asp492, Asp493 and His577 (Figure 1a). Later, the structure 1SK6 of EF bound to reaction products was obtained [10]. This structure displays two competing ion binding modes, involving one or two Ytterbium(III) ions (Figures 1c and 1d). As it was recognized that Yb(III) ions could favor single metal binding modes due to their high charge [9, 12], crystallization was attempted in the presence of Magnesium(II), the biological catalytic metal. Structure 1XFV was thus obtained [9], and two Mg^{2+} ions were observed in the catalytic site, as in mammalian adenylyl cyclases (MACs) [6].

(Figure 1)

However, the structure 1XFV displays several features different from the previous structures. First, the positions of the second Magnesium ion and conformation of the 3'-deoxy-ATP are substantially different (Figure 1b): Indeed, while one of the ions was observed in the central-ion binding site described above, the other was only coordinated by oxygens of the triphosphate group. Second, 3'-deoxy-ATP conformation (Figure 1b) was different from that of substrate in the crystal structures of MACs [6]. Third, structure 1XFV was obtained at 200 mM Mg^{2+} , a concentration much higher than that required to fully inhibit the enzyme [7]. On the other hand, a single Mg^{2+} ion was observed in structures 1XFW and 1Y0V [9], which were obtained by soaking reaction products in

a EF-CaM crystal. Alternative hypotheses can be drawn from these facts: (i) catalysis occurs in presence of one ion, (ii) a second magnesium is brought by ATP upon binding and dissociates after the reaction. Consequently, the biological significance of the two Mg^{2+} in structure 1XFV is unclear.

The preference for one or two-ion binding modes cannot be easily deduced from analysis of electrostatic interactions. As reaction products are negatively charged, two cations should stabilize the transition state, but more efficient product release is expected with a single cation. Indeed, maximal enzymatic activity is observed at physiological Mg^{2+} concentrations, of about 10 mM [13]. Similarly, high Ca^{2+} concentrations ($2 \mu\text{M}$) increase PPI affinity to the binding pocket, and the natural catalytic ion Mg^{2+} induces full EF inhibition at a concentration of 100 mM [7, 10]. Maximal enzymatic activity is observed at physiological Mg^{2+} concentrations, of about 10 mM [13].

We have previously studied equilibrium dynamics aspects of the EF-CaM complex, focusing 1) on the relationships between Ca^{2+} binding and CaM mobility [3] and CaM-EF interactions [4], and 2) on substrate and product conformations in the active site, and their relation to its ionic content [14]. In [3], it was shown that CaM acts as a spring to maintain EF open, which is dependent on the stability of the inter-linker region between the two CaM lobes. We have further shown that this EF-CaM interactions modulate Ca^{2+} affinity to CaM [4]. The role of the substrate and product conformations and ionic binding modes in the active site was probed in [14]: the ATP docking to the active site in structure 1K90 in the presence of single ion, is more rigid relative to the two- Mg^{2+}

binding mode observed in 1XFV. At the same time, a two-Mg²⁺ binding site also impairs product mobility, thus supporting a one-ion binding mode [14].

In the present work, we focus on non-equilibrium aspects of EF function: the dynamics of reactant and product dissociation from the active site. A combination of non-conventional molecular dynamics simulations techniques allows to study general aspects of ligand release and to highlight the important interactions that have to be broken upon ligand dissociation.

2 Materials and Methods

2.1 System preparation and equilibration

Structures of EF-CaM complexes with different ligands were used: (i) 1K90 with a 3'-deoxy-ATP and one Ytterbium(III) ion [1]; (ii) 1XFV with 3'-deoxy-ATP and two Mg²⁺ ions [9]; (iii) 1SK6 with reaction products cyclic-AMP and PPi, with two alternative ion configurations including either one or two ions Yb³⁺ [10].

Yb³⁺ ions were replaced by Mg²⁺, the actual catalytic ion, and the 3'-hydroxyl missing in 3'-deoxy-ATP was added. Missing residues in 1K90 (loop between K768 and F773) and in 1SK6 (loops between S674 and V694 and between Q767 and F773) were modeled based on the corresponding coordinates of 1XFV structure.

CHARMM27 force field was used for proteins, ions, and ATP [15, 16]. Parameters for PPi and cyclic-AMP (cAMP) were derived from analogous groups in the CHARMM27

set, with Merz-Kollman charges computed using Gaussian03 [17] from the optimized geometries at the 6-31G(d,p) level of theory. The TIP3P model [18] was used for water.

One or two hydrogen atoms were added to PPI structure of minimum energy calculated with Gaussian03, in order to obtain PPIH and PPIH₂. In PPIH, the proton was put on the phosphate oxygen closer to Mg²⁺ ions, and pointing to the solution. In PPIH₂ hydrogen atoms were added to both phosphate groups of PPI (Figure 7a). New charges were computed using single-point Gaussian03 calculations for PPIH and PPIH₂ at the same level of theory than for PPI. Geometry optimization was not used at this step because it led to unreasonable structures for protonated species in vacuum.

Structures were solvated with 25,000 water molecules yielding a water shell at least 10 Å thick (protein images being at least 20 Å apart). Water molecules and sodium ions required to neutralize the system were placed with Packmol [19, 20]. VMD [21] and Pymol [22] were used for visualization and preparation of figures.

Energy minimizations and simulations were performed with NAMD [23]. The following protocols were used for equilibration: (i) total system energies were minimized with 2000 steps of conjugate gradients, keeping the protein, ligand and protein-bound ions fixed, except for modeled residues in 1K90 and 1SK6, (ii) with the same atoms fixed, a 100 ps MD was performed with constant-pressure constant-temperature conditions (NPT), with Langevin pistons and bath to control pressure and temperature with coupling periods of 1 ps (iii) the side-chains of the proteins were allowed to move in a 500 steps conjugate gradient minimization followed by a 100 ps of NPT MD (iv) the final equilibration step

was a 100 ps NPT MD without any restraint. A cutoff of 12 Å was used for non-bonded interactions along with force shifts to smooth the interaction transition at the cutoff distance, as implemented in NAMD [23]. Temperature was set to 298.15 K and the pressure to 1 Bar. A 2 fs time-step was used and hydrogens constrained with RATTLE [24].

The final equilibrated systems were boxes of approximate dimensions of $120 \times 80 \times 80$ Å containing about 85,000 atoms. All production runs were performed from the final coordinates of the equilibrated systems, as described below.

2.2 Notation

The following notations will be used to describe results. We refer to crystal structures by their PDB entries in upper case, ie. 1SK6, 1XFV and 1K90. The Mg^{2+} ion coordinated by the three binding pocket residues Asp492, Asp493 and His577 is called “central- Mg^{2+} ”, or “cMg”. An ion in this position was observed in each crystallographic structure (Figure 1): in 1K90, in 1XFV, and in the one-ion binding mode of 1SK6. The second ion observed in the 1XFV structure, mostly coordinated by the phosphate group of ATP, is called “non-central- Mg^{2+} ” (Figure 1b). The Mg^{2+} ions placed at the positions of Yb^{3+} ions in the two-ion binding-mode of 1SK6 structure (Figure 1c) were called MgC and MgP for those closer to cAMP and PPi respectively.

MD systems built from 1XFV contain either the central- Mg^{2+} only (1xfv-cMg) or the two Mg^{2+} (1xfv-Mg2). One MD system containing one Mg^{2+} (1k90) was derived from

1K90. Simulations of reaction products were performed from structure 1SK6 with four different ionic binding modes. One mode contains only the central-Mg²⁺ and is referred as 1sk6-cMg. The system with the single Mg²⁺ ion closest to PPI is called 1sk6-MgP. Similarly, the system for which only the Mg²⁺ closest to cAMP is present is called 1sk6-MgC. Finally, the system with both MgP and MgC is called 1sk6-Mg2. Table 1 provides the system names as well as their basic components.

(Table 1)

2.3 Ligand dissociation simulations

Ligand dissociation usually occurs in time-scales not accessible to MD simulations and, thus, non-conventional simulation methods are required. For the study of ligand dissociation, several methods exist: Enhanced Sampling methods, which modify in the force field reducing energy barriers to accelerate the dynamics, as LES (see below) or Accelerated Molecular Dynamics [25], or induction methods, as SMD (see below) or Targeted Molecular Dynamics [26], in which additional forces are introduced to promote dissociation through specified channels or pathways. Here we chose LES and SMD as complementary techniques, the first providing non-biased but approximate dissociation paths, and SMD, in which dissociation is promoted through the paths observed with LES without interfering in intramolecular or intermolecular energy terms. Therefore, we are able to provide both an overall description of the dissociation pathways, and mechanistic details.

2.3.1 Locally Enhanced Sampling simulations

Locally Enhanced Sampling (LES) simulations were proposed by Elber and Karplus and originally applied to carbon monoxide escape from myoglobin [27]. The method is designed to study molecular motions of some subset of a large molecular system. To obtain a broader conformational sampling, simulations are performed with multiple replicas of the subset of interest, in presence of a unique copy of the environment. This method has been extensively used to study ligand diffusion through globins, and several results were confirmed experimentally [28–30]. Dissociation of larger molecules in other ligand-receptor complexes have also been studied [31, 32].

To study ligand dissociation from a ligand-protein complex with LES, the ligand is replicated. Replicas do not interact with each other, and protein-ligand interactions are divided by the number of replicas, according to the scheme described in [31]. The probability of observing a dissociation event is increased because there are several copies of the ligand and because reduction of ligand-protein interactions result in exponentially increased dissociation rates [33].

LES simulations were performed with CHARMM version 33b2 [34]. The solvent was modeled implicitly in LES simulations by the use of simplified long-range interactions: a distance-dependent dielectric (RDIE option in CHARMM) and a force shift at a distance of 8 Å are combined, in order to fit globally a sigmoid shape [35] for the dielectric constant (1.416). A switching function is applied to van der Waals interaction from 7 to 8 Å. This

modeling avoids difficulties of simulating interactions between multiple copies and explicit solvent molecules and can be used here because the LES simulations are only intended to provide dissociation trajectories to guide the SMD simulations setup.

Equilibrated conformations, described above, were used as initial coordinates. The solvent was removed and multiple copies of ATP, PPi or cAMP were inserted according to the system studied. 22 runs for each system were performed with a varying number of ligand copies of 1, 2, 4, 8, 10, 12, 14, 16, 18, 20, 22, 24, 26, 28, 30, 32, 35, 40, 45, 50, 55 or 60. Independent LES simulations were performed with multiple copies of cAMP, PPi and ATP. A ligand was considered as dissociated if all its atoms were farther than 8 Å from the center-of-mass of Asp491, Asp493 and His577 at the end of the run.

LES simulations were performed to study the dissociation of ATP in 1k90, 1xfv-cMg and 1xfv-Mg2 systems, and the dissociation of cAMP and PPi in 1sk6-cMg and 1sk6-Mg2 systems.

2.3.2 Steered Molecular Dynamics simulations

In Steered Molecular Dynamics (SMD) simulations, ligand dissociation is induced by an external force [36, 37]. The pulling direction can be chosen from considerations on the protein structure, as the presence of cavities, or from educated guesses [36]. Here we use dissociation directions observed in LES simulations as a guide. An advantage of LES directions, in addition to avoiding a biased choice of pulling directions, is that they allow a more exhaustive mapping of possible dissociation routes. Indeed, as LES simulations

facilitate the dissociation, they can probe difficult routes, as well as most likely ones. The combination of LES and SMD techniques has been successfully used in previous studies of ligand dissociation from Thyroid Hormone Receptors [32, 38].

SMD simulations were performed with the same protocols as the equilibration of the systems, and initiated from the configuration obtained after equilibration. The SMD force is designed to gently dissociate ligands [36, 37]: the pulling force \vec{F} has the form $\vec{F} = k(\vec{v}t - \Delta\vec{x})$, where k is the force constant, \vec{v} is the pulling direction, $\Delta\vec{x}$ is the displacement vector of the pulled group from its initial position, and t is the simulation time. The actual displacement, $\Delta\vec{x}$, adjusts to the target one, $\vec{v}t$, depending on the interactions of the pulled group with the environment. Therefore, the force is constantly modulated by the resistance encountered upon dissociation, allowing to analyze local structural features affecting the dissociation path and pulling force [36, 37].

The pulling force was applied to all atoms of the groups according to a mass weighted scheme for pulling, as implemented in NAMD [23]. The force constant was $4.0 \text{ kcal mol}^{-1} \text{ \AA}^{-2}$ which is sufficiently stiff to promote noticeable variations of the force with 1-2 \AA displacements of the pulled group [36, 38]. The pulling velocity was initially varied between 0.2 and $0.0125 \text{ \AA ps}^{-1}$. The breaking of tight ligand-ion interactions persisted as the major step towards dissociation (as will be discussed), and the force profiles were qualitatively similar, unless for longer dissociation times (Figure 2). Therefore, the most important characteristics of dissociations events were unaltered. Thus, the fastest pulling rate was used, and to improve sampling multiple pulling directions were chosen as described below.

All protein atoms farther than 20Å from the active site were kept fixed in order to avoid protein translations and rotations.

We have also performed Targeted Molecular-Dynamics simulations [25] of all crystallographic models (1k90, 1xfv-Mg2 and 1sk6 with one or two ions) using the same initial configurations as the ones used for SMD and final ligand positions obtained using LES. In TMD, the external force is introduced to promote the transition from a initial to a target structure by applying a time-dependent restraint on the pulled atoms which depends on the RMS deviation from the target position. The overall sequence of events observed in SMD were confirmed by these auxiliary simulations (See Supplementary Information).

(Figure 2)

The following dissociations were studied (Table 1): (i) dissociations of PPi and cAMP from 1sk6-cMg and 1sk6-Mg2, (ii) dissociations of PPIH and PPIH₂ from 1sk6-Mg2, (iii) ATP dissociation from 1k90, 1xfv-cMg and 1xfv-Mg2. Dissociation of PPi, PPIH, PPIH₂ and cAMP were performed in presence of the other reaction products. Additional dissociations of cAMP and PPi were made in absence of each other from 1sk6-Mg2 and 1sk6-MgC, respectively. For each dissociation, five different pulling directions were applied to represent the paths observed with LES and to provide a more robust analysis.

To summarize, a total of 85 independent runs were performed for 17 different systems, to give a total SMD simulation time of approximately 130 ns, including equilibration runs. Each run took approximately 10 days per nanosecond, summing a total of about

43 months of CPU time, distributed on a cluster running CentOS Linux 4.3.

3 Results

3.1 Analysis of dissociation paths with LES

ATP dissociation occurs for a number of copies larger than 20 in 1k90, larger than 8 in 1xfv-cMg and larger than 18 in 1xfv-Mg2 (Table 2). This suggests that dissociation is easier in 1xfv-cMg. However, the total number of dissociation events is similar for 1k90 and 1xfv-cMg, and smaller for 1xfv-Mg2.

(Table 2)

cAMP dissociation is already observed in simulations with 8 copies, whereas PPI release was only observed for more than 35 copies (Table 2). Total number of dissociations is also smaller for PPI than for cAMP, whatever the system analyzed, 1sk6-cMg or 1sk6-Mg2. Thus, cAMP seems to dissociate more easily than PPI.

The total number of dissociation events for PPI is larger in 1sk6-Mg2 (42, Table 2) than in 1sk6-cMg (26, Table 2), and the minimum number of copies required to observe dissociation is smaller.

For cAMP dissociation, the minimum number of copies required for dissociation increases from 8 to 14 from the one to the two-Mg²⁺ binding modes. The total number of dissociation events decreases from 545 to 144. Impaired dissociation with two Mg²⁺ can

be explained by additional electrostatic attraction experienced by the negatively charged cAMP. Further details of dissociation mechanisms will be discussed below based on SMD simulations.

ATP dissociations do not follow paths through a single well-defined channel, and occur more or less randomly between switch C and helix D (Figure 3a). By contrast, PPi and cAMP dissociate through solvent-accessible channels laying in opposite sides of the protein structure. These channels can be discerned in crystallographic structures (see protein surfaces in Figures 3b and 3c) [10], and show that ligands are solvent accessible. Both channels are located between Switch C and Helix D, on the helical domain side for PPi (Figure 3b), and on the calmodulin side for cAMP (Figure 3c). As the channels are on opposite sides, PPi and cAMP can dissociate independently.

(Figure 3)

3.2 Dissociation analysis by SMD simulations

3.2.1 Profiles of forces and interactions during product dissociation

Highest force barriers for cAMP dissociation were obtained in simulations where it forms tight interactions with Mg^{2+} ions: 1sk6-Mg2 and 1sk6-MgC (Figure 4a). The lower forces required for dissociation in other single-ion simulations (Table 3) indicate that pulling forces are dominated by cAMP-MgC interactions. Similar forces are required to induce PPi dissociation when the MgP ion is present (1sk6-Mg2 and 1sk6-MgP, Figure 5a).

The Mg^{2+} ions farther from the substrates have relatively marginal roles in dissociation barriers.

(Table 3)

(Figure 4)

(Figure 5)

Interaction energies of products with Mg^{2+} ions in the active site may either vanish smoothly, break abruptly, or persist, as shown in Figures 4b and 5b.

These interactions persist if the ion leaves the catalytic pocket bound to the dissociating product. PPI has a stronger tendency to dissociate with a bound Mg^{2+} ion than cAMP: MgP ion always follows PPI in 1sk6-Mg2 and 1sk6-MgP, as revealed by persistent MgP-PPI interaction energies (Figure 5b). By contrast, the MgC ion dissociates in only one of five cAMP dissociation runs in 1sk6-Mg2 (Figure 4b).

Breaking of tight product-ion interactions occurs abruptly, as observed for cAMP-MgC interactions in four 1sk6-Mg2 cAMP dissociation runs (Figure 4b). Interaction with the MgP ion in the same simulation also vanishes abruptly, although from a higher baseline. Similar profiles are observed for MgC ion in PPI dissociation runs of 1sk6-Mg2 (Figure 5b).

Conversely, product-ion interactions vanish smoothly for weak interacting Mg^{2+} ions. In these cases, the forces required for dissociation are smaller and the ions remain in the catalytic site (PPI dissociation runs in 1sk6-cMg and 1sk6-MgC, Figure 5b, and in cAMP dissociation in 1sk6-cMg and 1sk6-MgP, Figure 4b).

Summarizing, the force profiles of cAMP and PPi dissociation are dominated by few tight electrostatic interactions with Mg^{2+} ions. The joint dissociation of one Mg^{2+} with the product is plausible, particularly if the ion is bound to a highly charged PPi. PPi protonation can attenuate these electrostatic interactions, as it will be discussed below.

3.2.2 Influence of solvation on product dissociation

Dissociation of ligands with tight electrostatic interactions (cAMP-MgC or PPi-MgP) is correlated with the increased solvation of catalytic site Mg^{2+} ions (1sk6-Mg2 and 1sk6-MgC in Figure 4c and 1sk6-Mg2 and 1sk6-MgP in Figure 5c) and to high pulling forces (Figure 4a and Figure 5a). Conversely, for cAMP dissociations in absence of MgC and PPi dissociations in absence of MgP, Mg^{2+} solvation remains essentially constant (Figure 4c: 1sk6-cMg and 1sk6-MgP; Figure 5c: 1sk6-cMg and 1sk6-MgC).

PPi solvation increases (Figure 5f) while PPi-protein interactions are preserved (Figure 5e). This results in more favorable overall interactions energies between the dissociating group and the environment (Figure 5d). Minimum energy is reached when pulling forces are maximal. Similar but more subtle trends can be observed for cAMP (Figures 4d-f).

As the strongest electrostatic bonds are broken, the products dissociate and solvation increases. However, it does not does not compensate for the loss of interactions with EF-CaM. This suggests that dissociation is driven by diffusion from this point on.

Ligand solvation increases while they are attached to the active site thanks to mecha-

nisms of tail detachment and catalytic site distortions. Detachment of cAMP tail occurs as follows: while the strong electrostatic coordination of the phosphate group is maintained, pulling drives partial dissociation of sugar and base groups, which become solvent exposed (as illustrated by the snapshots taken from a cAMP dissociation simulation from 1sk6-Mg2 in Figure 6a). The number of water molecules solvating cAMP increases from 20 to about 55 in this step, with a moderate effect in solvation energy, as less polar groups of cAMP are solvated first.

(Figure 6)

PPi dissociation follows a similar mechanism. One phosphate group is attached directly to the cations in the active site, while the other is bound to Lysines 353 and 372 (Figure 6b, from a PPi dissociation run from 1sk6-Mg2). The phosphate closer to the catalytic ions remains attached, while the other moves towards the solvent. The catalytic site passes through local distortions that facilitate the exposure of PPi to solvent (Figure 6b). Indeed, Aspartates 492 and 493, that coordinate the central Mg^{2+} ion, are located in a loop, which can move towards the solvent facilitating the access of water molecules to charged sites. This distortions may be overestimated by pulling forces, but some degree of loop flexibility facilitating ligand release is plausible. Once water insertion substitutes interactions of products with the protein and Mg^{2+} ions, the products diffuse into water.

To summarize, solvation plays an important role in product dissociation, which occurs in two phases: products are partially solvated, then product-complex interactions are

lost and dissociation takes place by diffusion. The flexibility of the active site facilitates solvation during the first step.

3.2.3 Effect of PPi protonation state

Since ion-product interactions are dominated by electrostatics, they can be significantly attenuated by ligand protonation. PPi, being small and highly charged, should be most sensible to this effect. For instance, protonation has been suggested as a mechanism to turn pyrophosphate a better leaving group for the nucleophilic reaction [39].

One or two protons were added to PPi leading to PPiH and PPiH₂. The proton of PPiH was added to the phosphate group closer to the Mg²⁺ ion, in order to maximize the charge effect. Protons of PPiH₂ were added in either phosphate group (Figure 7a). Charges were computed independently for each protonation state, and protonation reduces the overall charges and individual oxygen atom charges, as shown in Figure 7a. We studied protonated-PPi dissociation in 1sk6-Mg2, in which electrostatic interactions are maximal.

(Figure 7)

Dissociation of PPi is facilitated by protonation (Figure 7b). The maximum force average required to extract PPi from 1sk6-Mg2 is 2924 pN. It is reduced to 2594 pN for PPiH and to 2263 pN for PPiH₂ (Table 3). Force integrals follow a similar trend. However, protonation does not fully compensate tight ligand-Mg²⁺ interactions: removing PPi in 1sk6-cMg is still significantly easier than PPiH₂ from 1sk6-Mg2 (Figure 7b).

Protonation of PPI can also facilitate dissociation by reducing its interactions with several basic residues located in the binding site, particularly Lysines 346, 353 and 372.

Protonation of PPI strongly affects its ability to drag Mg^{2+} ions during dissociation. While one Mg^{2+} follows PPI in every dissociation run of 1sk6-Mg2, this only happened twice in five PPIH dissociation runs, and never with PPIH₂. Therefore, the balance between Mg^{2+} -product and Mg^{2+} -active site interactions changed, and Mg^{2+} tends to remain bound to carboxylates of Asp491 and Asp493 rather than to dissociate.

3.2.4 Product dissociation as independent events

Experimental data suggests that at low Ca^{2+} concentration dissociation of products is ordered and that PPI dissociates first [10]. By performing dissociation simulations of one product in absence of the other, we intended to investigate whether the mechanisms of dissociation are cooperative.

PPI dissociation in absence of cAMP was performed in 1sk6-Mg2 binding mode, since cAMP dissociations, described above, suggest that ions do not dissociate with cAMP. The maximum force average required to dissociate PPI in absence of cAMP is smaller (2596 pN) than in its presence (2924 pN, Table 3 and Figure 8). This difference is within the standard deviations of both sets (220 and 868 pN respectively).

(Figure 8)

cAMP dissociation in absence of PPI was performed in 1sk6-MgC, as MgP appeared

above to always dissociate along with PPI. By contrast, the maximum force average for cAMP dissociation is the same in presence (2062 pN) or absence (2076 pN) of PPI.

Thus, from the present simulations it is not possible to discern a clearly cooperative mechanism of dissociation. PPI dissociation seems to be slightly facilitated by cAMP anticipated release, probably because of increased flexibility and solvent-accessibility of the half-empty active site. Nevertheless, the effect is small relative to the influence of other structural features of the binding cavity (as the number of ions, for instance).

3.2.5 ATP dissociation

ATP dissociation was studied in 1k90, 1xfv-cMg and 1xfv-Mg2. Largest force barriers (Figure 9a) are obtained in 1k90, and reach frequently 2600 pN. By contrast, the forces surpass 1500 pN in only one 1xfv-cMg run.

(Figure 9)

ATP interaction with the whole environment (protein, water and ions) (Figure 9d) becomes monotonically less attractive. Thus, ATP appears to form more favorable interactions in the active site than in water, suggesting a favorable enthalpy of binding.

Dissociation of ATP in 1k90 results in an abrupt breaking of ATP-cMg interactions in three runs (Figure 9b). In two other runs these interactions do not vary, as Mg^{2+} and ATP dissociate jointly. Breakage of ATP- Mg^{2+} interactions is essential to ATP attachment to the binding site, as their breakage is correlated with force release (Figure 9a).

By contrast, in 1xfv-cMg, interactions of ATP with the central-Mg²⁺ are smoothly lost (Figure 9b), and the cation never dissociates. A similar profile is observed for the central-Mg²⁺ ion in 1xfv-Mg2, whereas the non-central-Mg²⁺ always leaves the binding pocket bound to ATP (Figure 9b). These observations suggest that the central-Mg²⁺ was part of the active site in 1XFV before ATP binding, while the non-central-Mg²⁺ was bound to ATP prior to complexation with EF.

In 1k90, breaking of ATP-Mg²⁺ interactions is dependent on the solvent accessibility of the active site. This access is evaluated by the number of water molecules solvating the Mg²⁺ ions (Figure 9c). Initially, ATP is bound to the ion and to EF, and the ion is totally protected from solvent (the number of water molecules is zero). In the course of the simulation, two water molecules substitute the Mg²⁺ interactions with ATP or with the protein. In three runs where the ion remains in the active site, the ATP-Mg²⁺ interactions are substituted by water molecules, whereas in the two runs where Mg²⁺ dissociation is observed, the active-site-Mg²⁺ interactions are replaced instead. Similar observations can be done in 1xfv-cMg and 1xfv-Mg2 simulations.

To summarize, ATP is more tightly attached to 1k90 than to 1xfv-cMg or 1xfv-Mg2. In 1k90, ATP-Mg²⁺ interactions are strong, and accompanied by strong Mg²⁺-protein interaction. The enzyme seems to make the best use of the ion to bind the reactant. In 1xfv-cMg and 1xfv-Mg2, on the other side, the central-Mg²⁺ ion is already accessible to solvent in crystallographic structure 1XFV, resulting in weaker ligand binding. Neither Mg²⁺ seems to be used optimally to bind ATP, one being bound too tightly to the protein,

the other being bound too tightly to the phosphate tail of ATP. This picture is coherent with observations made in equilibrium simulations, in which the 1K90 binding mode displayed a more rigid ATP docking and stronger ATP-cMg²⁺ interactions [14].

Discussion

LES simulations provide the first dynamical analysis of EF substrate and product dissociation, and confirm the hypothesis that release of products occurs through different solvent accessible channels [10]. These channels are located at opposite sides of the protein. ATP dissociation, on the other side, display no preference for any channel in our simulations.

Forces required to dissociate PPi are larger those required to remove cAMP in agreement with experimental K_i values [10]. Protonation of PPi has two effects: (i) the pulling forces decrease significantly, (ii) the balance of ionic interactions is changed, and probabilities of Mg²⁺ dissociation are reduced. Therefore, protonation facilitates ligand release, and affects the mechanism of product and ion dissociation from the active site. This observation could be experimentally probed by analyzing the pH dependence of product release. Indeed, EF activity is pH-dependent, and this effect is usually associated to deprotonation of the O3' oxygen at high pH [9]. However, even higher proton concentrations inhibit EF activity [11], and deprotonation of products could account for this effect.

The present work also provides insights into the mechanisms of ATP binding and dissociation with one or two Mg²⁺ ions. A two-metal-ion catalytic mechanism is commonly

accepted for DNA and RNA polymerases [5], and has also been strongly supported by several crystal structures of Mammalian Adenylyl Cyclases (MACs) [6]. In the catalytic site of polymerases [40], the first ion binds the active site with the nucleotide phosphate, and the second ion enters the pocket when with the nucleotide docked [5, 39]. EF may not follow a mechanism identical to that of polymerases [39] or mammalian adenylyl cyclases (MACs) [6]. Indeed, this bacterial toxin has a different biological function: while polymerases and MACs physiologically control their reactions, EF function is to overproduce cAMP to disturb cell signaling, consistently with its much higher catalytic rate relative to MACs [10].

EF-CaM crystal structure 1XFV, which contains two ions, was obtained at Mg^{2+} concentration much higher than that required to inhibit the enzyme. Therefore, the two-ion binding mode may not be representative of the functional state. The high ionic concentration could induce binding of the central- Mg^{2+} to EF prior to ATP association impairing correct docking of ATP and leading to EF inhibition. 1xfv simulations support this view, as the non-central- Mg^{2+} is attached to ATP and dissociates jointly with it, while the central- Mg^{2+} ion remains bound to the active site. Conversely, in 1k90 simulations, Mg^{2+} ions are shared between ATP and the protein, optimizing binding. The hypothesis of an incorrect ATP docking in 1XFV is also supported by ATP structure in 1K90: it resembles the conformation observed in MACs, agrees with the positions of the products in 1SK6, and displays a more rigid docking of ATP [14].

Dissociation of products also support an one-ion catalytic site, since dissociation of

negatively charged products is facilitated. Barriers for ligand dissociations are clearly correlated with breaking of electrostatic interactions to Mg^{2+} ions, and subtle displacements of ions in the binding pocket have large effects on barrier heights. We hypothesize that displacements of Mg^{2+} ions in the active site could facilitate ligand dissociation. After the reaction and formation of PPI and cAMP, the ion Mg^{2+} previously bound to ATP in 1k90 would be mobile and could occupy different positions: (i) bound to PPI (MgP), (ii) the central position (cMg), or (iii) bound to cAMP (MgC). As MgP or cMg, it would facilitate cAMP dissociation, and as MgC or cMg, facilitate PPI release. Noticeably, cMg favors the dissociation of both products. Alternatively, as MgP, the ion could leave the binding site bound to PPI. A mobile ion in the active site can also explain the electron densities observed in the three different positions in structure 1SK6.

Finally, it is interesting to compare the study of dissociation with previous equilibrium simulations [14]. In equilibrium runs, conformational drifts of products cAMP and PPI are significantly increased when the one- Mg^{2+} 1SK6 is considered, relative to the two- Mg^{2+} 1SK6 mode [14]. This is because the tight ligand- Mg^{2+} interactions strongly attach cAMP and PPI to the binding site, as observed here. In the single ion binding mode, indeed, water insertion within the ligand- Mg^{2+} interface was observed for cAMP, leading to partial detachment from the active site. The strong Mg^{2+} ATP interaction in 1K90 also significantly stabilizes ATP relative to 1XFV models. Therefore, equilibrium simulations support the conclusions that tight ligand- Mg^{2+} interactions are essential for ligand affinity and that they must be replaced by water molecules for ligand dissociation. On the

other hand, during the partial dissociation of cAMP observed in equilibrium runs, water insertion and the detachment of cAMP's phosphate group occurred before the displacement of the adenosine group [14]. Therefore, without pulling, water has additional time to penetrate within ligand-Mg²⁺ interactions inducing dissociation, such that alternate sequences of events with the phosphate group detaching first are possible.

Conclusion

In this work we performed a molecular level investigation of the mechanisms of ATP and product dissociation from the active site of the Anthrax Edema Factor. By using a combination of non-conventional simulation techniques, we are able to provide both the overall sequence of events of ligand dissociation and mechanistic details. ATP dissociation requires significant exposure of the active site, while PPi and cAMP dissociate through solvent accessible cavities that are visible in opposite sides of the EF-CaM complex.

ATP dissociation is harder in the 1K90 binding mode. Dissociation of the central-Mg²⁺ bound to ATP is observed in 1k90, but not in 1xfv-cMg or 1xfv-Mg2. This suggests that the central-Mg²⁺ ion in 1XFV was bound to the active site prior to ATP association, which can explain EF inhibition at high Mg²⁺ concentration. 1k90 simulations show that the central-Mg²⁺ ion should bind the active site associated with ATP, and that possible incorporation of a second ion, if it occurs, is a subsequent step.

Product dissociation is greatly dependent on interactions with Mg²⁺ ions. These

interactions must be substituted by interactions with water upon ligand dissociation. Dissociation of products, particularly of PPI, seems to occur in two steps: first, the solvation of the leaving group increases, while most important electrostatic interactions with the active site are preserved. As most important active site residues belong to loop regions, the flexibility of the active site certainly plays an important role in this step. Finally, ligand-protein interactions are broken, and products dissociate by diffusion into solvent. Protonation of PPI favors dissociation, providing a complementary interpretation for the pH dependence of EF activity.

3.2.6 Acknowledgements

LM thanks the Brazilian Coordenação de Aperfeiçoamento de Pessoal de Nível Superior (CAPES), for financial support. Institut Pasteur and CNRS are acknowledged for funding.

References

1. Drum CL, Yan SZ, Bard J, Shen Y, Lu D, Soelaiman S, Grabarek Z, Bohm A, Tang WJ. Structural basis for the activation of anthrax adenyl cyclase exotoxin by calmodulin. *Nature* 2002;415:396–402.
2. Ulmer TS, Soelaiman S, Li S, Klee CB, Tang WJ, Bax A. Calcium dependence of the interaction between calmodulin and anthrax edema factor. *J Biol Chem* 2003;278:29261–29266.

3. Laine E, Yoneda JD, Blondel A, Malliavin TE. The conformational plasticity of calmodulin upon calcium complexation gives a model of its interaction with the oedema factor of *Bacillus anthracis*. *Proteins* 2008;71:1813–1829.
4. Laine E, Martínez L, Blondel A, Malliavin TE. Activation of the edema factor of *Bacillus anthracis* by calmodulin: Evidence of an interplay between the EF-calmodulin interaction and calcium binding. *Biophys. J.* 2010;99:2264–2272.
5. Steitz TA, Smerdon SJ, Jager J, Joyce CM. A unified polymerase mechanism for nonhomologous DNA and RNA polymerases. *Science* 1994;266:2202–2025.
6. Tesmer JJ, Sunahara RK, Johnson RA, Gosselin G, Gilman AG, Sprang SR. Two-metal-ion catalysis in adenylyl cyclase. *Science* 1999;285:756–760.
7. Shen Y, Lee YS, Soelaiman S, Bergson P, Lu D, Chen A, Beckingham K, Grabarek Z, Mrksich M, Tang WJ. Physiological calcium concentrations regulate calmodulin binding and catalysis of adenylyl cyclase exotoxins. *EMBO J* 2002;21:6721–6732.
8. Arndt JW, Zhong W, Gong X, Showalter AK, Liu J, Dunlap CA, Lin Z, Paxson C, Tsai MD, Chan MK. Insight into the Catalytic Mechanism of DNA Polymerase β : Structures of Intermediate Complexes. *Biochemistry* 2001;40:5368–5375.
9. Shen Y, Zhukovskaya NL, Guo Q, Florian J, Tang WJ. Calcium-independent calmodulin binding and two-metal-ion catalytic mechanism of anthrax edema factor. *EMBO J* 2005;24:929–941.

10. Guo Q, Shen Y, Zhukovskaya NL, Florian J, Tang WJ. Structural and Kinetic Analyses of the Interaction of Anthrax Adenyl Cyclase Toxin with Reaction Products cAMP and Pyrophosphate. *J Biol Chem* 2004;279:29427–29435.
11. Gupta M, Alam S, Bhatnagar R. Kinetic characterization and ligand binding studies of His351 mutants of *Bacillus anthracis* adenylate cyclase. *Archiv Biochem Biophys* 2006;446:28–34.
12. Brautigam CA, Ascheim K, Steitz TA. Structural elucidation of the binding and inhibitory properties of lanthanide (III) ions at the 3'-5' exonucleolytic active site of the Klenow fragment. *Chem Biol* 1999;6:901–908.
13. Nelson DL, Cox MM. *Lehninger Principles of Biochemistry*. New York, USA: W.H.Freeman & Co Ltd; 2008.
14. Martínez L, Laine E, Malliavin T, Nilges M, Blondel A. ATP conformations and ion binding modes in the active site of anthrax edema factor: A computational analysis. *Proteins* 2009;77:971–983.
15. MacKerell AD, Bashford D, Bellott M, Dunbrack RL, Evanseck JD, Field MJ, Fischer S, Gao J, Guo H, Ha S, Joseph-McCarthy D, Kuchnir L, Kuczera K, Lau FTK, Mattos C, Michnick S, Ngo T, Nguyen DT, Prodhom B, Reiher WE, Roux B, Schlenkrich M, Smith JC, Stote R, Straub J, Watanabe M, Wiorkiewicz-Kuczera J, Yin D, Karplus

- M. All-atom empirical potential for molecular modeling and dynamics Studies of proteins. *J Phys Chem B* 1998;102:3586–3616.
16. Pavelites JJ, Bash PA, Gao J, MacKerell AD. A Molecular Mechanics Force Field for NAD⁺, NADH and the Pyrophosphate Groups of Nucleotides. *J Comput Chem* 1997;18:221–239.
17. Frisch MJ, Trucks GW, Schlegel HB, Scuseria GE, Robb MA, Cheeseman JR, Montgomery, Jr JA, Vreven T, Kudin KN, Burant JC, Millam JM, Iyengar SS, Tomasi J, Barone V, Mennucci B, Cossi M, Scalmani G, Rega N, Petersson GA, Nakatsuji H, Hada M, Ehara M, Toyota K, Fukuda R, Hasegawa J, Ishida M, Nakajima T, Honda Y, Kitao O, Nakai H, Klene M, Li X, Knox JE, Hratchian HP, Cross JB, Bakken V, Adamo C, Jaramillo J, Gomperts R, Stratmann RE, Yazyev O, Austin AJ, Cammi R, Pomelli C, Ochterski JW, Ayala PY, Morokuma K, Voth GA, Salvador P, Dannenberg JJ, Zakrzewski VG, Dapprich S, Daniels AD, Strain MC, Farkas O, Malick DK, Rabuck AD, Raghavachari K, Foresman JB, Ortiz JV, Cui Q, Baboul AG, Clifford S, Cioslowski J, Stefanov BB, Liu G, Liashenko A, Piskorz P, Komaromi I, Martin RL, Fox D J, Keith T, Al-Laham MA, Peng CY, Nanayakkara A, Challacombe M, Gill PMW, Johnson B, Chen W, Wong MW, Gonzalez C, Pople JA. Gaussian 03, Revision C.02. Gaussian, Inc., Wallingford, CT, 2004.
18. Jorgensen WL, Chandrasekhar J, Madura JD, Impey RW, Klein ML. Comparison of simple potential functions for simulating liquid water. *J Chem Phys* 1983;79:926–935.

19. Martínez JM, Martínez L. Packing optimization for automated generation of complex system's initial configurations for molecular dynamics and docking. *J Comput Chem* 2003;24:819–825.
20. Martínez L, Andrade RA, Birgin EG, Martínez JM. Packmol: A package for building initial configurations for molecular dynamics simulations. *J Comput Chem* 2009;30:2157–2164.
21. Humphrey W, Dalke A, Schulten K. VMD - Visual Molecular Dynamics. *J Molec Graphics* 1996;14:33–38.
22. DeLano WL. The PyMOL Molecular Graphics System. 2002;DeLano Scientific, Palo Alto, CA, USA:<http://www.pymol.org>.
23. Phillips JC, Braun R, Wang W, Gumbart J, Tajkhorshid E, Villa E, Chipot C, Skeel RD, Kale L, Schulten K. Scalable molecular dynamics with NAMD. *J Comput Chem* 2005;26:1781–1802.
24. Andersen HC. RATTLE - A velocity version of the SHAKE algorithm for molecular dynamics calculations. *J Comp Phys* 1983;52:24–34.
25. Chirsten M, van Gunsteren WF. On searching in, sampling of, and dynamically moving through coformational space of biomolecular sytems: A review. *J Comp Chem* 2008;29:157–166.

26. Schlitter J, Engels M, Kruger P. Targeted Molecular Dynamics - A new approach for searching pathways of conformational transitions. *J Mol Graph* 1994;12:84–89.
27. Elber R, Karplus M. Enhanced sampling in molecular dynamics: Use of the Time-Dependent Hartree approximation for a simulation of carbon monoxide diffusion through myoglobin. *J Am Chem Soc* 1990;112:9161–9175.
28. Gibson QH, Regan R, Elber R, Olson JS, Carver TE. Distal pocket residues affect picosecond ligand recombination in myoglobin: an experimental and molecular dynamics study of position 29 mutants. *J Biol Chem* 1992;267:22022–22034.
29. Scott EE, Gibson QH, Olson JS. Mapping the pathways for O₂ entry into and exit from myoglobin. *J Biol Chem* 2001;267:5177–5188.
30. Brunori M, Gibson QH. Cavities and packing defects in the structural dynamics of myoglobin. *EMBO Rep* 2001;2:674–679.
31. Blondel A, Renaud JP, Fischer S, Moras D, Karplus M. Retinoic acid receptor: a simulation analysis of retinoic acid binding and the resulting conformational changes. *J Mol Biol* 1999;291:101–115.
32. Martínez L, Sonoda MT, Webb P, Baxter JD, Skaf MS, Polikarpov I. Molecular dynamics simulations reveal multiple pathways of ligand dissociation from thyroid hormone receptors. *Biophys J* 2005;89:2011–2023.

33. Ulitsky A, Elber R. The thermal equilibrium aspects of the time dependent Hartree and the locally enhanced sampling approximations: formal properties, a correction, and computational examples for rare gas clusters. *J Chem Phys* 1993;98:3380–3388.
34. Brooks BR, Bruccoleri RE, Olafson BD, States DJ, Swaminathan S, Karplus M. CHARMM - A program for macromolecular energy, minimization, and dynamics calculations. *J Comp Chem* 1983;4:187–217.
35. Lavery R, Sklenar H, Zakrzewska K, Pullman B. The flexibility of the nucleic acids: (II). The calculation of internal energy and applications to mononucleotide repeat DNA. *J Biomol Struct Dyn* 1986;3:989–1014.
36. Kosztin D, Izrailev S, Schulten K. Unbinding of retinoic acid from its receptor studied by steered molecular dynamics. *Biophys J* 1999;76:188–197.
37. Isralewitz B, Baudry J, Gullingsrud J, Kosztin D, Schulten K. Steered molecular dynamics investigations of protein function. *J Mol Graph Model* 2001;19:13–25.
38. Martínez L, Webb P, Polikarpov I, Skaf MS. Molecular dynamics simulations of ligand dissociation from thyroid hormone receptors: Evidence of the likeliest escape pathway and its implications for the design of novel ligands. *J Med Chem* 2006;49:23–26.
39. Castro C, Smidansky E, Maksimchuk KR, Arnold JJ, Korneeva VS, Gotte M, Konigsberg W, Cameron CE. Two proton transfers in the transition state for nucleotidyl

transfer catalyzed by RNA- and DNA-dependent RNA and DNA polymerases. Proc Natl Acad Sci USA 2007;104:4267–4272.

40. Liu J, Tsai MD. DNA Polymerase β : Pre-Steady-State Kinetic Analyses of dATPS Stereoselectivity and Alteration of the Stereoselectivity by Various Metal Ions and by Site-Directed Mutagenesis. Biochemistry 2001;40:9014–9022.

Tables

Name	Components	Dissociation of
1sk6-Mg2	1SK6 with the Mg ²⁺ ions MgP and MgC	PPi, cAMP, PPIH, PPIH ₂ , PPi in the absence of cAMP, PPi using variable pulling velocities, cAMP using variable pulling velocities
1sk6-cMg	1SK6 with the central-Mg ²⁺ (cMg)	PPi, cAMP
1sk6-MgP	1SK6 with the Mg ²⁺ ion closest to PPi (MgP)	PPi, cAMP
1sk6-MgC	1SK6 with the Mg ²⁺ ion closest to cAMP (MgC)	PPi, cAMP, cAMP in the absence of PPi
1k90	1K90 model with the central-Mg ²⁺ (cMg)	ATP, ATP using variable pulling velocities
1xfv-Mg2	1XFV model with two Mg ²⁺ ions	ATP
1xfv-cMg	1XFV model with the central-Mg ²⁺ (cMg)	ATP

Table 1: Nomenclature of simulated systems. For each system and dissociation studied, five independent runs of 1 ns are recorded to provide a LES or SMD simulation. cMg indicates the Mg²⁺ ion bound in the central position of the active site, coordinated by Asp492, Asp493 and His57. MgP and MgC refer to Mg²⁺ positions closest to PPi and cAMP, respectively.

System	Ligand		
	PPi	cAMP	ATP
1k90	-	-	20/242
1xfv-cMg	-	-	8/227
1xfv-Mg2	-	-	18/156
1sk6-cMg	40/26	8/545	-
1sk6-Mg2	35/42	14/144	-

Table 2: Minimum number of copies for which dissociation was observed and total number of dissociation events observed for each ligand in each LES simulation (minimum/total).

Ligand	System	Maximum (SD)	Integral (SD)
ATP	1k90	2290 (282)	857 (252)
	1xfv-cMg	1318 (181)	346 (20)
	1xfv-Mg2	1147 (67)	298 (39)
cAMP	1sk6-cMg	841 (68)	176 (13)
	1sk6-Mg2	2139 (197)	488 (74)
	1sk6-MgP	725 (93)	160 (23)
	1sk6-MgC	2062 (208)	498 (81)
	1sk6-MgC, no PPi	2076 (298)	424 (91)
PPi	1sk6-cMg	1419 (337)	334 (51)
	1sk6-Mg2	2924 (868)	828 (147)
	1sk6-MgP	2780 (296)	724 (96)
	1sk6-MgC	1066 (143)	271 (41)
	1sk6-Mg2, no cAMP	2596 (220)	636 (75)
PPiH	1sk6-Mg2	2594 (273)	624 (75)
PPiH ₂	1sk6-Mg2	2263 (187)	571 (81)

Table 3: Maximum and integrated forces required for dissociation of reactants and products, obtained from SMD simulations. Maximum forces are in pN and integrated forces are in $\text{pN}\times\text{ns}^{-1}$. Averages and standard deviations (SD) of five independent runs are shown.

Figures

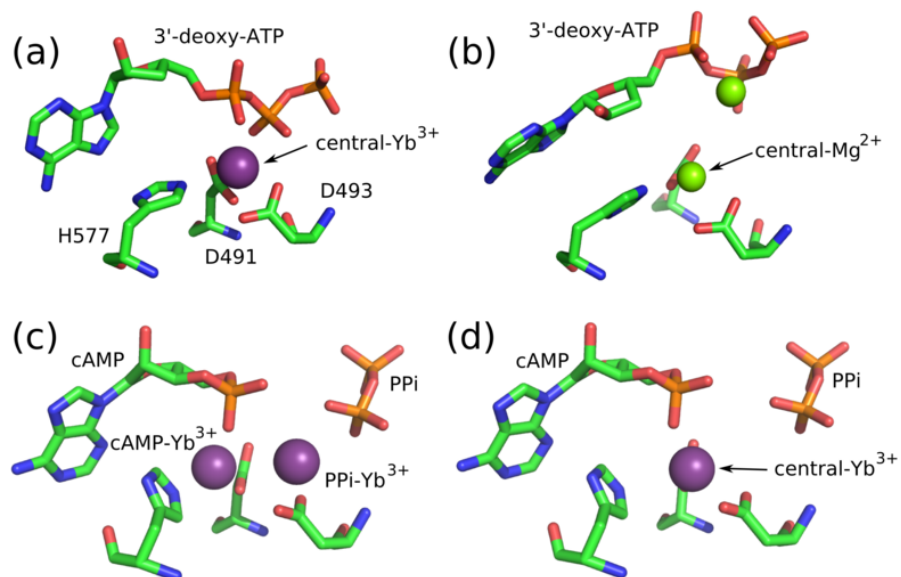


Figure 1: Binding modes of 3'-deoxy-ATP and products as observed in crystallographic structures. (a) 3'-deoxy ATP bound in presence of a single Yb³⁺ ion, from structure 1K90. (b) 3'-deoxy-ATP bound in presence of two Mg²⁺ ions from 1XFV. Product bound structures with (c) two Yb³⁺ or (d) one Yb³⁺ were suggested for the 1SK6 crystallographic model. For a global view of the EF-CaM complex see Figure 3.

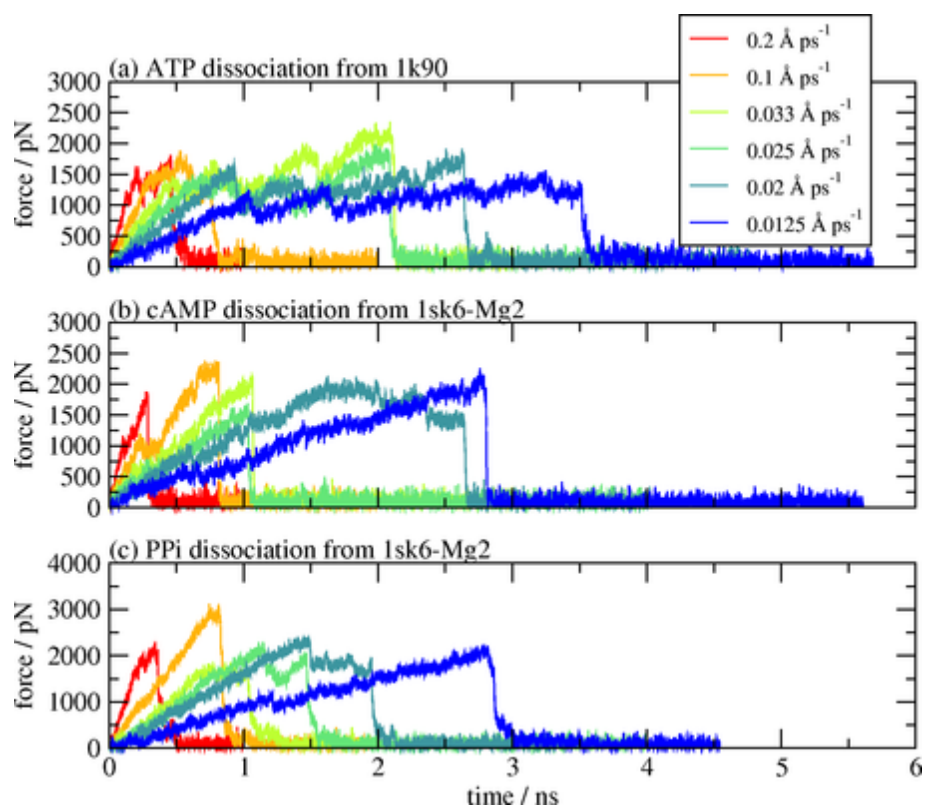


Figure 2: Force profiles for ligand and product dissociation using different velocities for pulling. Major barriers for dissociation are preserved.

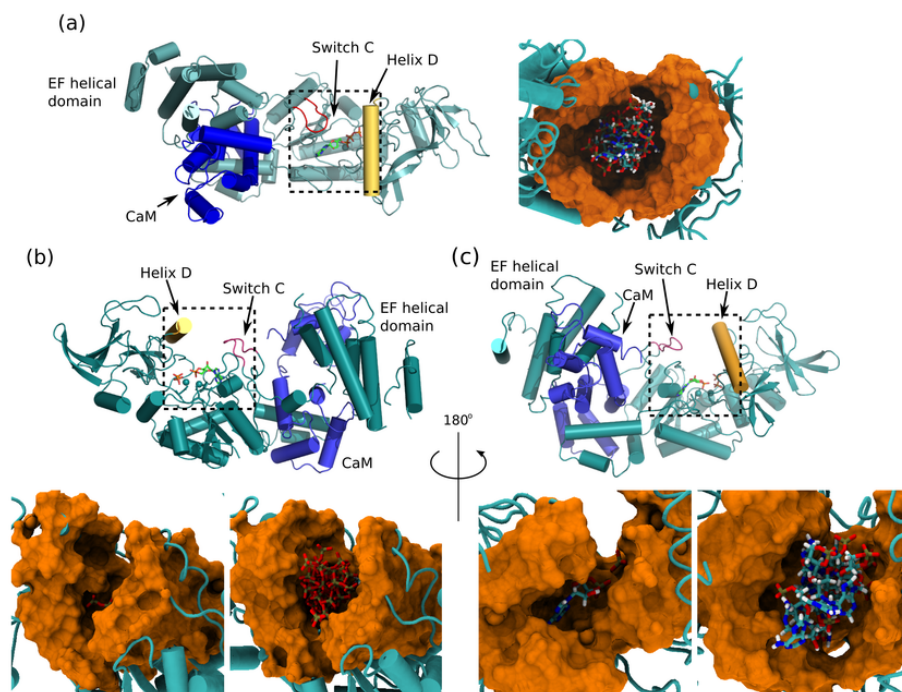


Figure 3: (a) ATP dissociation occurs by exposure of the active site, allowing ATP to escape in approximate random directions between Switch C and Helix D. Product dissociation occurs through different solvent accessible cavities, as observed in LES simulations. (b) PPI dissociation. (c) cAMP dissociation. Figures (b) and (c) represent the EF complex rotated 180° relative to each other. Surface images on the left show the cavities in the crystallographic models, the expansion of these cavities during ligand dissociation are displayed on the right. Helix D is drawn in yellow, Switch C in red, the remaining part of EF is in cyan and CaM in dark blue.

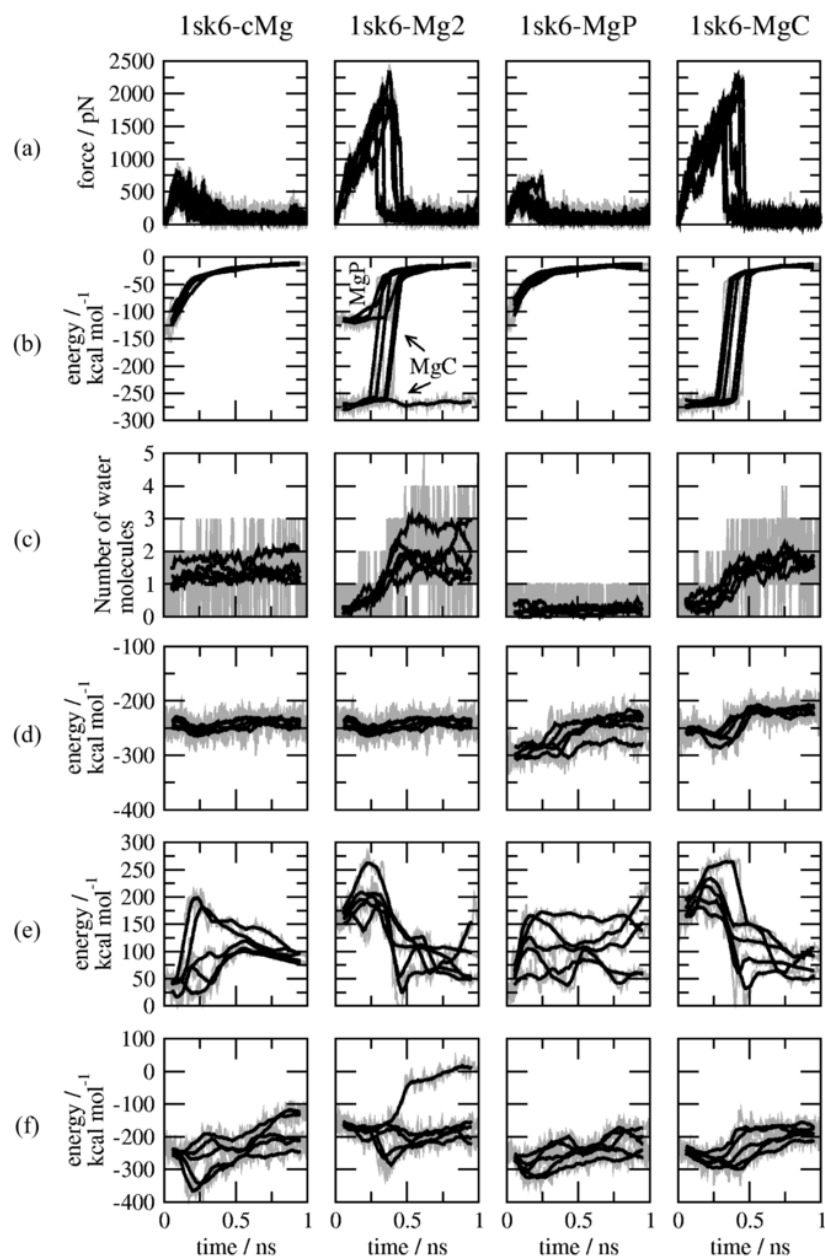


Figure 4: cAMP dissociation probed by SMD simulations: (a) Force required for cAMP dissociation. (b) Interaction energies of cAMP with Mg^{2+} ions. (c) Water molecules having an atom closer than 2 \AA from Mg^{2+} ions. Interaction energies of cAMP (d) with the whole environment, (e) with EF-CaM, (f) with water molecules.

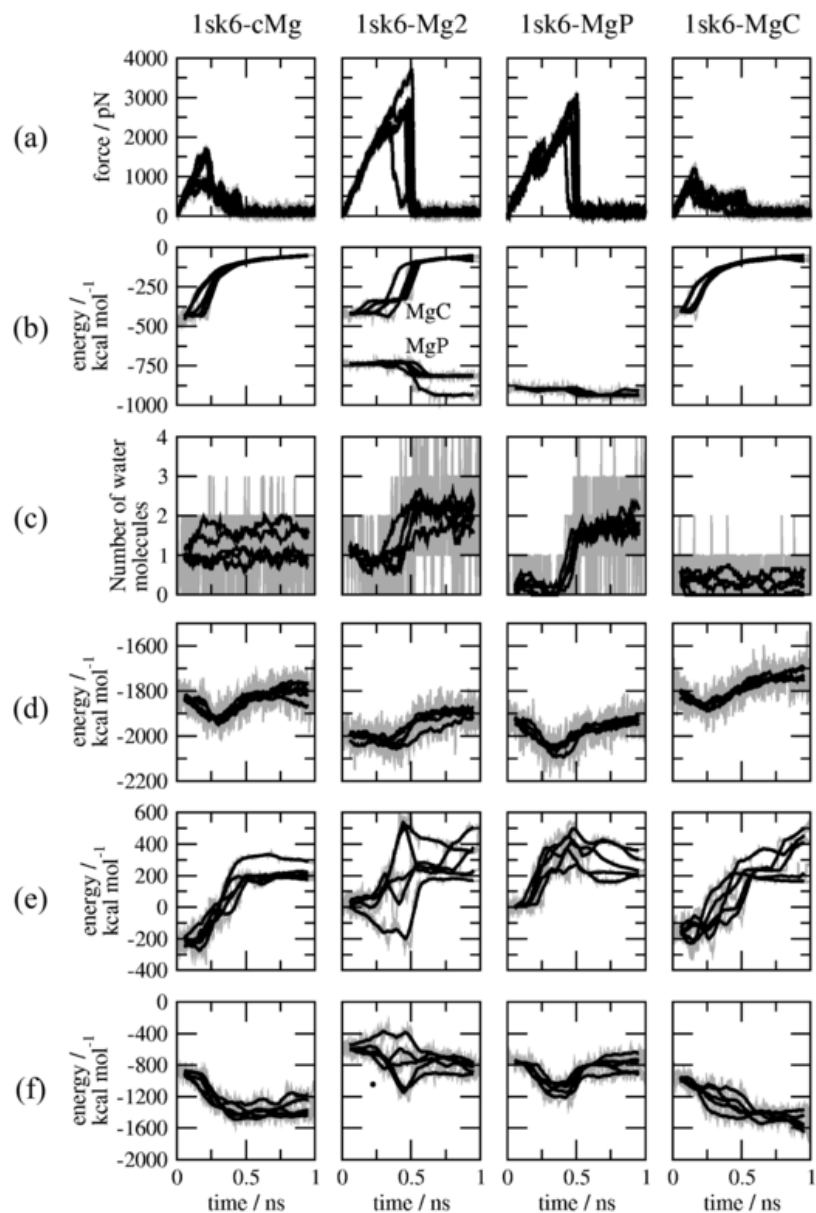


Figure 5: PPi dissociation probed by SMD simulations: (a) Force required for PPi dissociation. (b) Interaction energies of PPi with the Mg^{2+} ions. (c) Water molecules having an atom closer than 2 \AA from Mg^{2+} ions. Interaction energies of PPi with (d) the whole environment, (e) with EF-CaM, and (f) with water molecules.

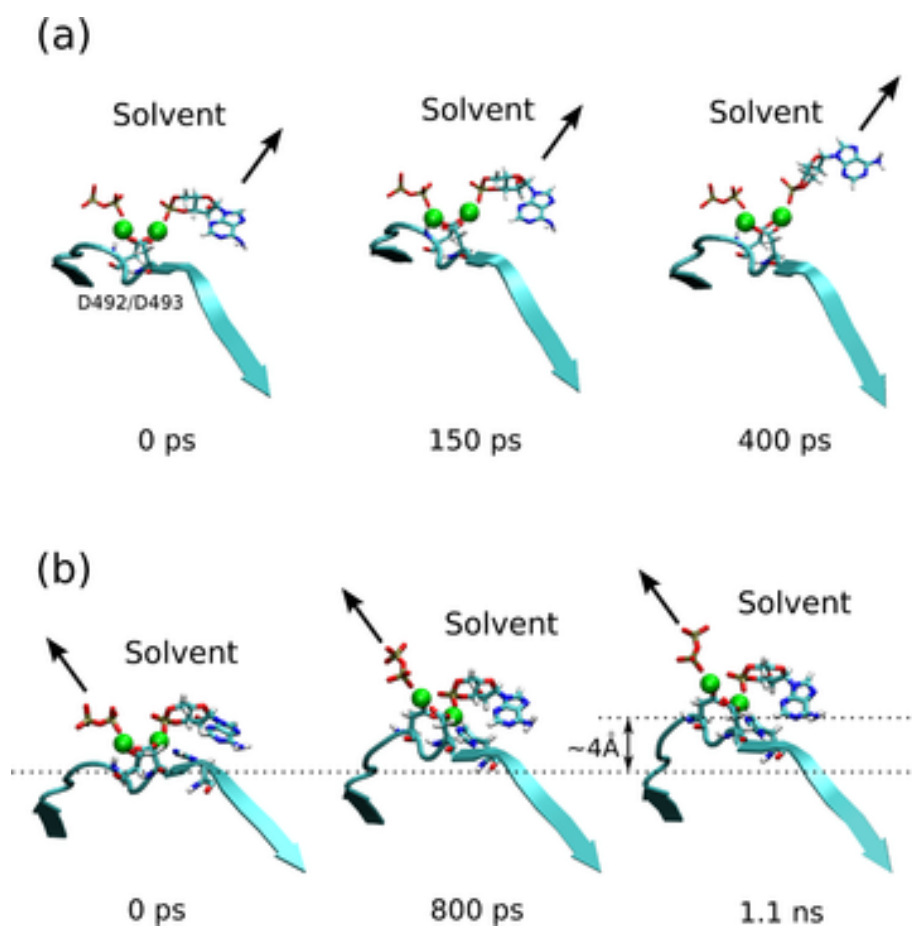


Figure 6: Movements allowing for improved solvation of ligands without breaking of their interactions with Mg^{2+} ions. The active site is exposed to solvent from the top. Arrows indicate pulling directions. (a) The adenine and ribose of cyclic-AMP are displaced by pulling while the phosphate remains attached to active site ions. (b) For Pyrophosphate, the same phenomenon is observed, but the group exposed to solvent is the phosphate not bound to ions. Final snapshots show the ligands just before breakage of product- Mg^{2+} interactions.

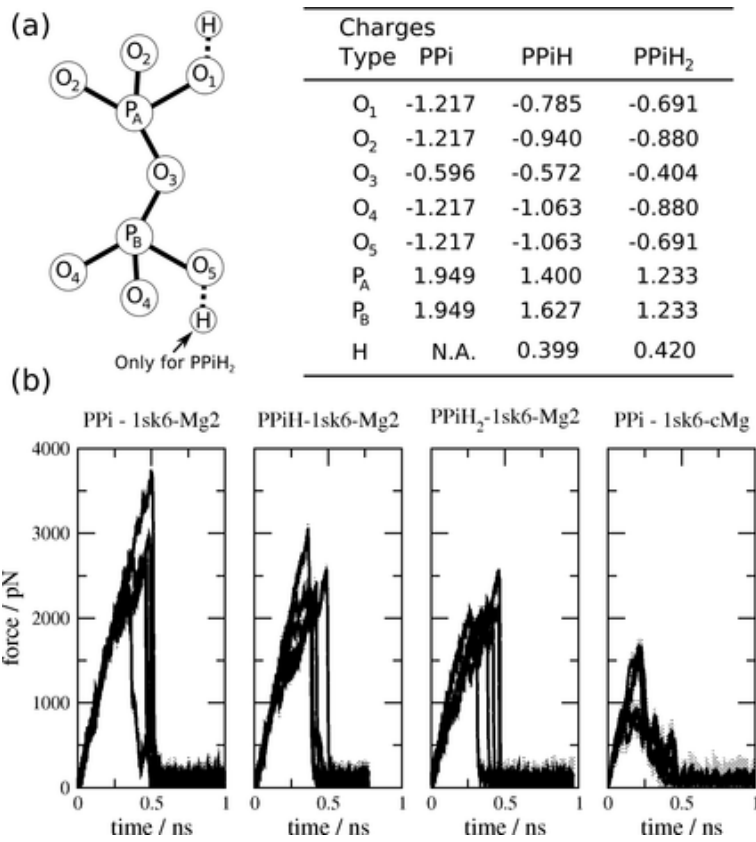


Figure 7: (a) Charges used for PPi dissociation simulations in different protonation states. (b) Forces required for PPi, PPIH and PPIH₂ dissociations in 1sk6-Mg2, and for PPi dissociation in 1sk6-cMg (PPi-1sk6-cMg).

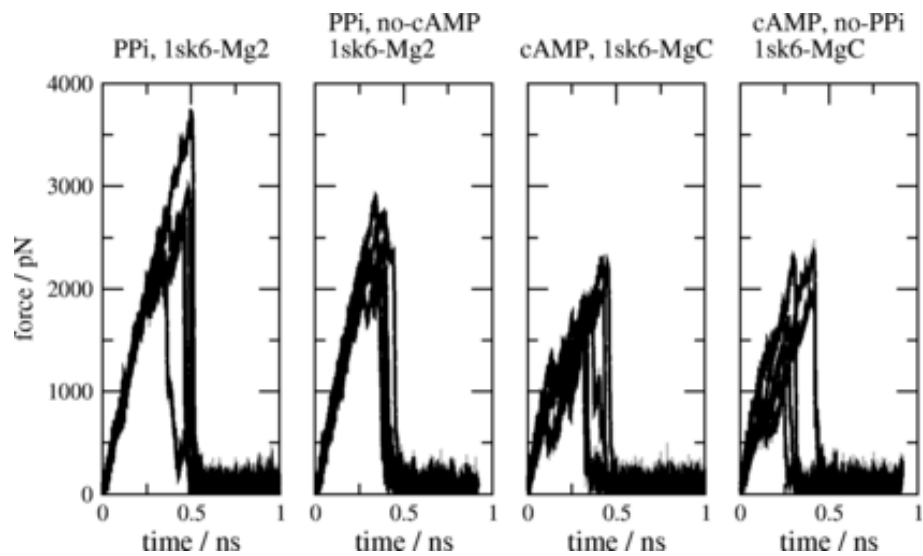


Figure 8: Force profiles observed during PPI and cAMP dissociation in absence of the other product (PPI no-cAMP 1sk6-Mg2, cAMP no-PPI 1sk6-MgC). These profiles are compared to the corresponding profiles obtained for dissociation of PPI and cAMP in presence of the other product (PPI 1sk6-Mg2, cAMP 1sk6-MgC).

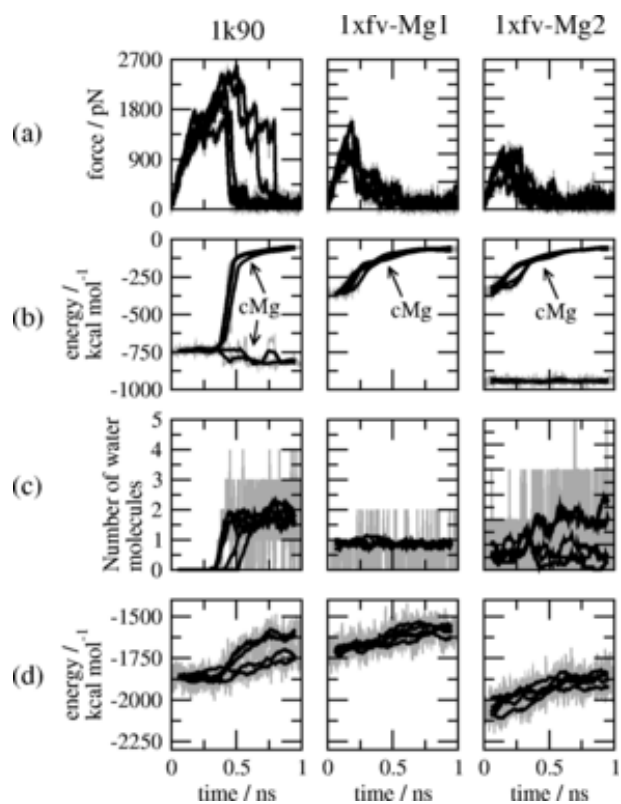


Figure 9: ATP dissociation probed by SMD simulations: (a) Forces as a function of time. (b) Interaction energies of ATP with Mg^{2+} ions. The cMg sign indicates the curves corresponding to the central- Mg^{2+} . (c) Number of water molecules having an atom closer than 2 \AA from the central- Mg^{2+} ion. (d) ATP interaction energy with the whole environment (protein, water molecules, ions).